Pacific Northwest National Laboratory
Operated by Battelle for the
U.S. Department of Energy

FY 2005 Quantum Cascade Laser Alignment System Final Report

T. L. Myers   B. T. Broocks
B. D. Cannon   T. L. Stewart
W. D. Wojcik   B. K. Hatchell

December 2005

DISCLAIMER

This report was prepared as an account of work sponsored by an agency of the United States Government. Neither the United States Government nor any agency thereof, nor Battelle Memorial Institute, nor any of their employees, makes **any warranty, express or implied, or assumes any legal liability or responsibility for the accuracy, completeness, or usefulness of any information, apparatus, product, or process disclosed, or represents that its use would not infringe privately owned rights**. Reference herein to any specific commercial product, process, or service by trade name, trademark, manufacturer, or otherwise does not necessarily constitute or imply its endorsement, recommendation, or favoring by the United States Government or any agency thereof, or Battelle Memorial Institute. The views and opinions of authors expressed herein do not necessarily state or reflect those of the United States Government or any agency thereof.

FY 2005 Quantum Cascade Laser Alignment System Final Report

T. L. Myers
B. D. Cannon
M. D. Wojcik
B. T. Broocks
T. L. Stewart
B. K. Hatchell

December 2005

Summary

The Alignment Lasers Task of Pacific Northwest National Laboratory's (PNNL's) Remote Spectroscopy Project (Project PL211I) is a co-funded project between DOE NA-22 and a Classified Client. This project, which began in the second half of FY03, involved building and delivering a Quantum Cascade (QC) Laser Alignment System to be used for testing the pupil alignment of an infrared sensor by measuring the response from four pairs of diametrically opposed QC lasers. PNNL delivered the system in FY04 and provided technical assistance in FY05 culminating into a successful demonstration of the system.

This project evolved from the Laser Development Task of PL211I, which is involved in developing novel laser technology to support development of advanced chemical sensors for detecting the proliferation of nuclear weapons. The laser systems are based on quantum cascade (QC) lasers, a new semiconductor source in the infrared. QC lasers can be tailored to emit light throughout the infrared region (3.5 – 17 µm) and have high output power and stability. Thus, these lasers provide an infrared source with superb power and spectral stability enabling them to be used for applications such as alignment and calibration in addition to chemical sensing.

The QC Laser Alignment System consists of four Alignment Source Assemblies (ASA's) with two QC lasers on each ASA and a computer control system with graphical user interface (GUI) for simple, reliable operation. Each ASA has a temperature sensor and heater for controlling the temperature to enable stable and reproducible output power. In addition, each laser has an on-board photodetector to measure the output power from the rear facet. The computer control system monitors the compliance voltage across the QC laser, the temperature, the current, and the signal from the optical detectors to ensure the system is operating within the specified tolerances.

The technical achievements for this project include 1) assembly and construction of the QC Laser Alignment System, 2) far-field characterization of all eight QC lasers, 3) delivery of the QC Laser Alignment System to the Using subcontractor in September 2004, and 4) successful demonstration of the QC Laser Alignment System in March 2005.

Contents

Figures

Tables

1.0   Laser Development Efforts

PNNL issued a subcontract to Maxion Technologies, Inc. to develop high performance quantum cascade (QC) lasers meeting the following performance characteristics:

1) Emit a single frequency near 1175 cm^{-1}.
2) Emit an average power from a single facet in excess of 5 mW.
3) Operate at a heat sink temperature greater than or equal to −50 ºC.

Maxion had already developed Fabry-Perot (FP) QC lasers emitting a comb of several evenly spaced frequencies near 1175 cm^{-1} with very good operating characteristics at cryogenic temperatures. They had also made significant progress with the development of single frequency devices under an existing PNNL contract by incorporating a distributed feedback (DFB) grating in the laser structure. To meet these performance characteristics, however, required substantially improved heat removal from the active region and were likely to require epi-down mounting of DFB QC laser devices. Due to the additional significant effort required, and the short time available, Maxion followed an aggressive technical approach that is described below in an attempt to achieve these objectives.

1.1   Technical Approach

Maxion investigated two approaches in parallel for achieving high-performance, epi-down-mounted DFB devices. Figure 1.1 illustrates the first approach.
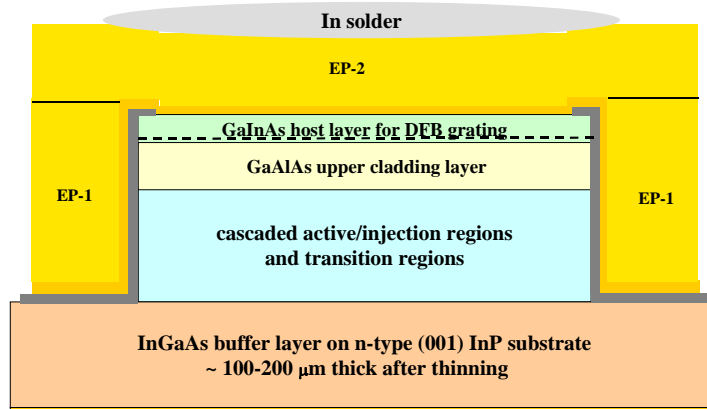
Figure 1.1.   QC DFB laser cross section showing top-mesa-etched grating covered with evaporated Au contact.

The figure shows the standard QC DFB laser structure mounted epi-side-down. Following MBE growth, a grating is etched into the laser sample. Mesas are then defined following the fabrication procedures used for epi-side-up DFB devices. After the device fabrication is nominally completed, additional Au will be deposited beyond the mesas to planarize the structure. This is accomplished by first covering the mesa top with a photoresist (PR) and then using the evaporated Au contact layers as electrodes to

electroplate (EP) additional Au onto the contact pads beyond the mesa (EP-1 in Figure 1.1). When the region beyond the mesa is filled with Au, the PR is removed and a second EP step adds additional Au to the overall structure, filling in any gaps that may have occurred near the mesa side walls (EP-2 in Figure 1.1). The device is then mounted epi-side-down with In solder to the Au-coated Cu heat sink, and the rear side of the substrate is contacted with wire bonds.

The second approach is shown in Figure 1.2 and relied on the regrowth of a low-loss, high-thermal conductivity InP cladding layer above the grating structure. In this case, the grating is etched closer to the device's active region.
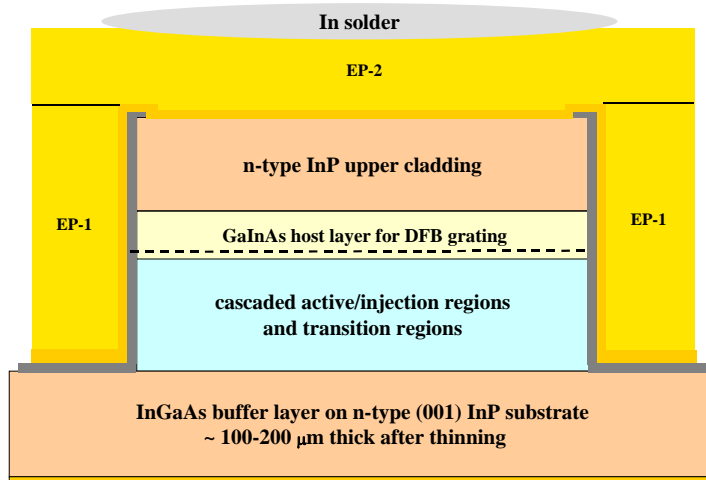
Figure 1.2. QC DFB laser cross section showing buried, etched grating covered with low loss InP cladding and evaporated Au contact.

Again, the mesa region is planarized for epi-side-down mounting of the device. This second approach is superior because the grating is closer to the active region providing for better coupling, and the metal contact layers are separated from the grating by a low-loss InP cladding layer. This separation between the contact and the optical mode will reduce optical losses improving performance at higher temperatures. The InP upper cladding also improves the thermal performance since InP has a higher thermal conductivity than InAlAs, which is the standard material used for the top cladding layer. In this approach, the laser sample is first grown by MBE through the active region and the GaInAs grating host layer. The sample is then removed from the MBE machine, and a grating is etched into the top surface. After appropriate cleaning, the sample will then be placed in another MBE machine or MOCVD system for regrowth of the additional n-type InP cladding and contact layers. Following the regrowth step, the metal contact will be evaporated and the same two EP steps described above for planarizing the device will be followed. The device will then be mounted epi-side-down as described above. Devices will be fabricated using both methods and tested extensively to ensure that performance objectives are met.

1.2   Device Performance Status

As of February 2004, Maxion had not yet demonstrated FP QCLs that operate cw at heat sink temperatures exceeding 223 K; the best FP devices that they have tested to date operated cw up to approximately 175K. Furthermore, the DFB QCLs generally underperformed their FP counterparts. The best DFB QCL (from a thermal perspective) operated cw up to 165K and showed a pulsed threshold current of 550 mA at a heat sink temperature of 220K. Some other DFB devices exhibited average output power (under pulsed conditions) between 1-3 mW at a 223K heat sink temperature.

The FP devices fabricated from four separate growth runs (in which the wafers are labeled as M62, M66, M191, and M192) that used standard AlInAs upper cladding layers and were mounted epi-side-up with thin Au contacts have actually performed quite well based on their pulsed threshold current densities at 80K and room temperature (RT) resistances. Maxion has found the RT resistance provides a good indicator of material quality, for if it is lower than previous devices that are based on the same design and that have performed well, a low value indicates inferior material quality. Modifications intended to improve FP performance including, for example, InP upper claddings (for reduced thermal resistance), epi-down mounting (for reduced thermal resistance) and HR coatings (for reduced threshold currents) have not yet demonstrated the expected performance improvements. Similar modifications with DFB devices have also failed to significantly improve performance, particularly at higher operating temperatures. This has led to questions regarding the laser material quality, the quality of device fabrication steps and procedures, and the high temperature effectiveness of the basic laser design.

1.2.1   Material Quality and Fabrication Procedures

Maxion assessed the device performance results and arrived at some conclusions regarding the adequacy of current laser material quality and current device fabrication procedures.

1)   The quality of the MBE QCL material. At first, Maxion had problems with many devices; their room temperature (RT) resistances were unusually low, and their 80K threshold currents were high. This was true for most devices fabricated from earlier growth runs, having top AlInAs claddings (M125, M127, M129, and M131) and InP-regrown upper claddings (M133, M137, and M139). They later traced part of this difficulty to a problem with the oxide desorption step used during the MBE growth of these samples. QCL samples M191 and M192 used a new oxide desorption procedure, and devices fabricated from these samples showed high RT resistances and low 80 K threshold currents. These devices were in every way comparable to the best QCLs previously made by Maxion (i.e. M62 and M66). The x-ray spectra, surface morphology, and RT resistance of FP devices fabricated from M191 and post-M191 device material (and having lattice-matched AlInAs upper cladding regions) were similar. Their present assessment is that all M191 and post M191 QCL material (whether intended for InP regrowth or not) is of high quality. For those post-M191 samples intended for InP regrowth, x-ray analysis prior to InP regrowth supports this assertion.

2) The quality of the InP regrown. The quality of InP material regrown on pre-M191 samples (e.g., M133, M137, and M139) is difficult to assess but was probably good. Although devices fabricated from these samples performed below expectations, this may have been caused entirely by the inferior oxide desorption procedures used on the growth of the underlying MBE material. The non-InP-based FP devices fabricated at the same time from similar samples using nominally identical desorption procedures (e.g., M125-M131) also performed poorly, with high threshold currents and lower RT resistances. Consequently, to some extent, these devices provide independent evidence to suspect inferior underlying MBE material. If they use only post-M192 growths to assess InP material quality (where new oxide desorption procedures were used during MBE growth), the InP quality has to be judged as mixed. M198 seems to be of good quality – its x-ray spectrum and surface morphology are good. But devices tested so far from later samples (M202, M203, and M204), are generally of poor quality. Unfortunately, no devices have yet been fabricated from M198 material – when M198 material was obtained from the MOCVD grower, Maxion tried to fabricate devices but discovered that the top InP layer was ~4 μm thick (rather than the expected 2.6 μm). By the time they were ready to fabricate M198 devices (which now required dry etching), the M202 sample was back from the MOCVD grower and ready for device fabrication. Consequently, Maxion deferred fabrication of the M198 devices and went forward with M202 device fabrication instead. The RT resistances from M202 devices were lower than expected, and device performance was unsatisfactory. While fabrication of additional M203 and M204 devices went forward, Maxion did some more x-ray work on pieces of M202 to better understand the poor performance. They discovered that the MOCVD-grown InP/InGaAs cap layer material was partially relaxed (very broad x-ray spectrum). This result was very surprising since the M198 sample's x-ray spectrum is sharp. They suspect that the poor performance of M203 and M204 devices is related to a similar degradation of device performance likely caused by the partially relaxed GaInAs/InP overlayers. Poor device performance is often the rule whenever relaxation is present since it generally can damage the underlying material.

3) The quality of the FP device fabrication steps. Quite generally, when FP devices are fabricated,   RT resistances are reasonably uniform and devices show similar performances. When new pieces from the same sample are fabricated into devices, similar results are obtained. They sometimes see increases in the variance of RT resistances from a group of neighboring devices as mesa widths decrease. They are not sure why this happens but suspect that the removal of photoresist (PR) after deposition of insulating layers is sometimes incomplete on samples with very narrow ridges. In any event, when RT resistance variances are large, new devices are fabricated. Consequently, they are reasonably confident that their fabrication procedures are reliable and that when problems arise, they can be easily spotted and corrected.

4) The quality of the DFB device fabrication steps. Initial grating fabrication procedures led to non- uniform grating-etch-depths. These problems were found to be due to a wider-than-expected PR edge-bead on samples used for device fabrication which caused misalignment problems between the sample (with PR layer) and the mask. New procedures for removing the edge-bead have led to very uniform PR layers and, consequently, more uniform grating grooves. All other fabrication steps used in DFB device fabrication mirror those used in the

fabrication of FP devices, and similar conclusions apply to the FP portion of the fabrication (described above).

At present, Maxion considers the quality of their fabrication of FP and DFB QC devices (from the MBE growth step to the fully fabricated device) to be limited only by the uncontrollable step connected with InP regrowth. They will not get high quality device performance if InP material regrowth is compromised in any way. The MOCVD grower has been informed of the problems and will address them in any future work.

1.3   Conclusions of Laser Development Efforts

Most of the work completed to date has been based on the Lucent 8.5 μm QCL design, both in the FP and DFB embodiments. Attempts to test modifications to the Lucent design (based on samples M203 and M204) have also been unsuccessful since available devices were likely damaged by partially relaxed InP upper cladding/GaInAs contact layers (both grown by MOCVD). No AlInAs-clad variants of these designs have yet been grown. The aggressive program plan followed to date was based on two central assumptions:

1) The Lucent design is adequate to meet the performance characteristics required for this project.
2) DFB devices would thermally outperform M62-like FP devices (based in part on the reduction expected in threshold currents when using a buried-grating QCL structure with InP upper cladding along with an HR coating, thick Au contacts, and epi-side-down mounting if needed, to further enhance DFB device performance).

The facts are that Maxion has not demonstrated a FP device based on the Lucent (or Maxion) design that has operated cw at 223 K, and no DFB device produced to date has thermally outperformed the M62-like FP device. Thus, a major failing of the work completed to date is its underlying premise that the Lucent design is adequate to meet the laser specifications and its adherence to the notion that a DFB device could outperform its M62-like partner FP device. There is simply no experimental evidence to support these assumptions. Maxion expected to achieve better QCL performance than they achieved with M62-like FP devices by applying HR coatings, InP claddings, and epi-down mounting to improve the thermal performance. To date, however, this strategy has failed.

In addition, the time pressure has led Maxion to omit development steps that might have revealed deeper problems earlier in the process. For example, fabricating simple Fabry-Perot lasers from each batch of material would have allowed verification of material quality and the basic laser design through characterization of the power, temperature and threshold current prior to using the material to fabricate more complicated DFB lasers. The additional fabrication steps required to produce a DFB laser caused further delays and may have also produced additional problems that prevented lasing or increased the threshold current. Maxion now believes the fundamental problems were with the initial poor material quality as well as an inadequate laser design for high temperature operation. Time could have been saved if these problems were identified prior to embarking on the DFB fabrication steps.

In view of these considerations, future work should *first* focus on demonstrating a new design (or modification to the existing Lucent design) that can achieve the necessary FP device performance. An objective would be to achieve cw performance from a FP device at or above a heat sink temperature of 280 K before working on DFB devices. After achieving the necessary FP milestone, fabrication and testing of DFB devices using the new design would then follow. Maxion would also need to compare lasers with InAlAs upper claddings and lasers with InP upper claddings that are otherwise identical to verify that InP regrowth is successful. The quality of the InP material can be determined through careful x-ray analyses of material returned by the MOCVD grower prior to having any processing work done on the returned samples. If InP material quality is lacking, the grower will repeat the work at no cost. If material problems continue to persist, another subcontractor can be used to regrow the necessary InP material. These steps, however, would take additional time and money to complete with no guarantee that Maxion would achieve their objectives.

Due to the time constraints, PNNL and the Client agreed to adjust the operating temperature from 223 K to 120 K. This step allowed Maxion to use laser material that they had already grown and begin mounting the lasers on the ASAs using standard epi-up mounting. The lasers were processed from M191, M192 and M307 wafers.

2.0   Alignment Source Assembly Design

This section details the mechanical and optical design of the alignment source assemblies (ASAs) used to meet the system specifications provided by the Client. Since this system is being used to test the alignment of an infrared instrument, the lasers need to provide a stable mode structure and output power. The specifications required that two lasers be mounted on each ASA with a 1" beam separation such that the ratio of output power between co-mounted lasers is constant within a tolerance band of ± 1%. Lasers mounted on separate ASAs need the ratio of output power to be constant within a tolerance band of ± 2.5%.

2.1   Mechanical Design

The mechanical mount needs to provide good thermal contact and efficient power dissipation to meet the stability requirements. Thus, PNNL used oxygen-free high conductivity (OFHC) copper to fabricate six ASA mounts. To increase the reliability of the thermal interface between the laser and the mount, PNNL incorporated a mounting scheme shown in Figure 2.1 with the lasers directly soldered to the OFHC copper mounting block.

With this design, the surface quality of the copper mounting block must be high and is discussed in more detail in Section 2.1.1. The lasers must also be soldered properly to the mounting block without any voids or overhang that could lead to detrimental heating effects. Unfortunately, whenever a laser failed to meet specifications, the entire ASA mount had to be returned to Maxion. Before a new laser could be soldered to the ASA, the wiring for all the components on the ASA had to be removed. Generally, it took a full day to wire up an entire ASA. Therefore, this entire process was time consuming. A better design would incorporate a sub-mount with an appropriate heat spreader, which would allow easy replacement of underperforming or damaged lasers.
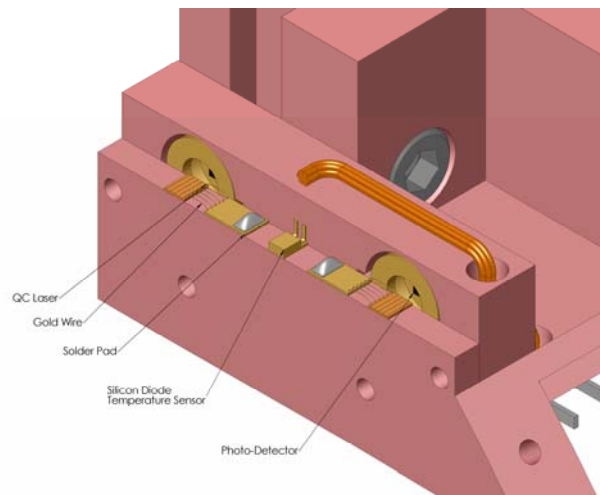

Figure 2.1. Mechanical Design for Optimal Power Stability

Reliable temperature control is crucial for power and wavelength stability. Thus, an on-board temperature sensor and a heater epoxied (TRA-BOND 2151) underneath the ASA mount are used for closed loop temperature control. The temperature sensor is mounted between the two lasers and on the same interface as the QC laser for improved performance. The temperature sensor is Lakeshore CX-1080. These sensors are fabricated from sputtered zirconium oxy-nitride thin films and mounted in a flat hermetic package. These thin film resistance sensors are very stable with repeated thermal cyling. The manufacturer quotes these sensors as having long-term stability of ±25 mK at 77 K and ±153 mK at 300 K.   The thermal response time is 0.25 s at 77 K and 0.8 s at 273 K, which is more than sufficient for this application. A four-lead sensor measurement scheme in which current leads and voltage leads are run separately up to the temperature sensor is used to eliminate the effect of lead resistance on the measurement.

This design also utilizes two on-board photodetectors to monitor the output power from the rear facet of each QC laser. These detectors can be used to provide an indicator that the lasers are emitting light at the specified power level. Their utility is discussed in more detail in Section 4.5.

2.1.1   Surface Quality of the ASA mounts

The surface quality of the laser mount is important to obtain good thermal contact between the QC laser and the heat sink, which affects the laser performance. PNNL measured the milled finish of two of the mounts using an optical profilometer. The unpolished surface of the ASA mount was so rough the profilometer had trouble measuring some of the features. Thus, PNNL polished the mounts to reduce surface roughness and increase thermal contact.

For comparison, PNNL measured the surface roughness of a standard copper mount near the footprint of the laser. Figure 2.2 shows the surface roughness of a standard Maxion QCL mount, which is a 1.5 cm x 0.75 cm x 3 mm copper block. The mounting surface of this block is simply polished using some fine grit sandpaper. The RMS roughness in this region is 112.7 nm.
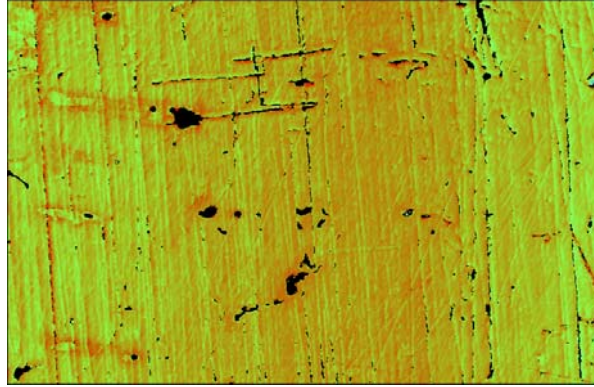
Figure 2.2. Profilometer scan of a standard mounting block received from Maxion. The large black splotch near the top of the image is 1.5 mm from the edge of the QC. The RMS roughness of this region is 112.7 nm.

Figure 2.3 demonstrates the first attempts at polishing the ASA mount. Although PNNL achieved excellent local flatness (~150 nm), the polishing technique led to extremely convex surface profiles. Figure 2.3b shows a large amount of curvature (> 7 μm) over the entire surface of the mount. This crowning is unacceptable for mounting lasers since it could lead to voids and detrimental heating effects that damage the laser.

a)

b)
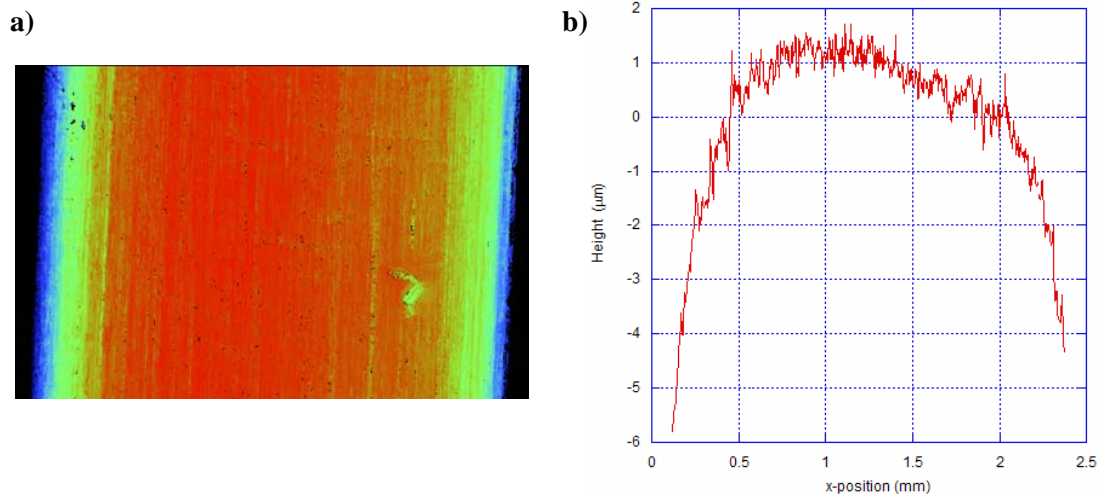
Figure 2.3. Example of preliminary attempts to polish the QC laser mount #1. a) A profilometer scan of the QC mount and b) A cut from Fig. 2.3.a demonstrating significant curvature of the surface.

Thus, PNNL devised a new technique to enable the laser mounting surface to be polished to a local flatness of ~100 nm and a total surface curvature between 300 and 550 nm. The new process involves using oversized brass jigs sandwiched around the copper mounting surface. These jigs serve two purposes. First they provide mechanical support for the thin copper mounting surface during the machining and polishing process. Second, during the polishing process, this setup prevents significant crowning of the copper surface by increasing the surface area to be polished,

which minimizes the relative angular deviation of the polishing block with respect to the laser mounting surface. PNNL is now able to achieve excellent flatness over the width of the mount and reduce the curvature over the entire surface. The results for three of the mounts are shown in Figures 2.4, 2.5 and 2.6. Similar results are obtained for the other three mounts. Mounts 3,4, 5, and 6 are used for ASAs A, B, C, and D respectively.

a)   b)
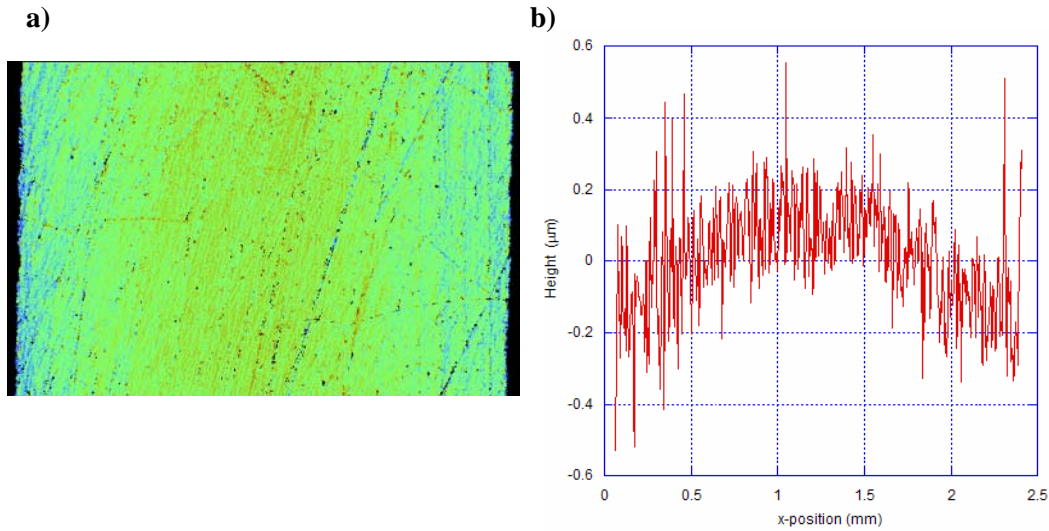
Figure 2.4.   Surface quality of mount #1 in the QC footprint region. *a*) A profilometer scan of the QC mount, and *b*) a horizontal cut from Fig. 2.4.a demonstrating reasonable flatness over the width of the mount.   The total curvature over the width of the mount is ~350 nm.

a)   b)
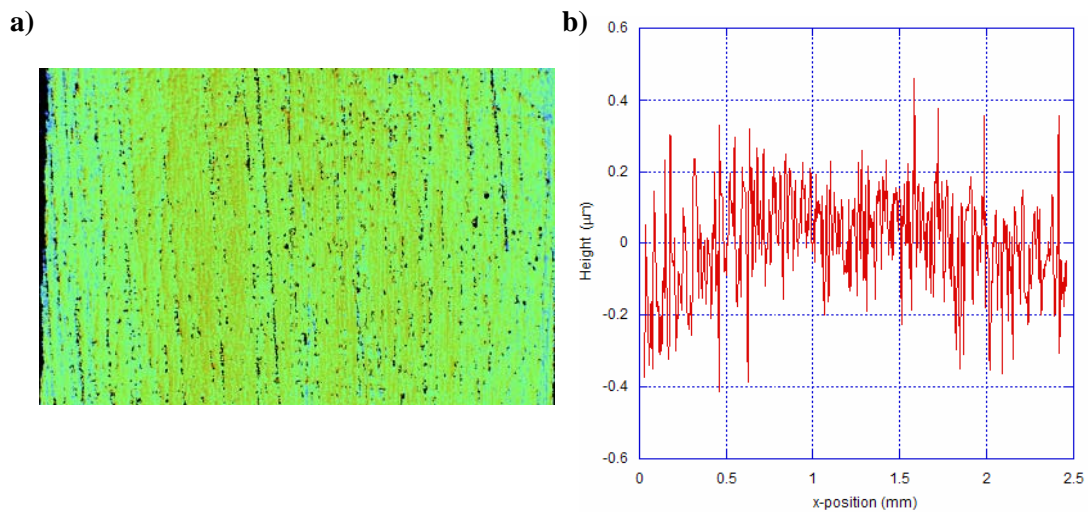
Figure 2.5.   Surface quality of mount #2 in the QC footprint region. *a*) A profilometer scan of the QC mount and *b*) a cut from Fig. 2.5.a demonstrating reasonable flatness over the width of the mount. The total curvature over the width of the mount is ~300 nm.

a)

b)
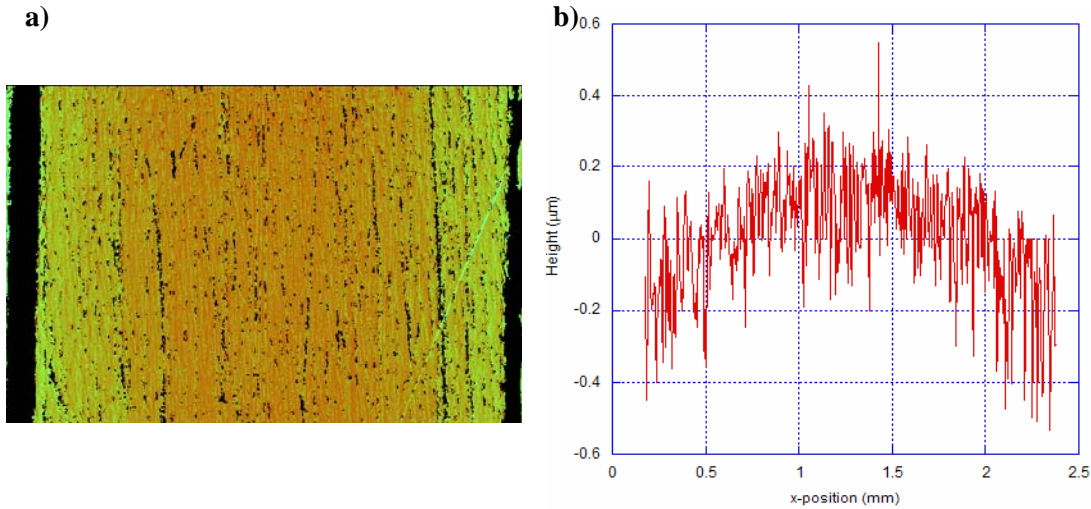
Figure 2.6. Surface quality of mount #3 in the QC footprint region. *a*) A profilometer scan of the QC mount and *b*) a horizontal cut from Fig. 2.6.a demonstrating reasonable flatness over the width of the mount. The total curvature over the width of the mount is ~500 nm.

2.2   Optical Design

The system specifications required the lasers have a stable 4° angular beam divergence measured by the full width at half maximum (FWHM). Figure 2.7 shows the ASA with the mini lens mount assembly used to obtain this specification. The lens assembly consists of a hemispheric Germanium lens with a 2 mm diameter and an AR coating at 8.5 μm mounted in a custom designed miniature XY translating mount fabricated from beryllium-copper alloy. Most of the lens mount is matched in thermal expansion to the copper plate to maintain alignment between room temperature and 80°K.
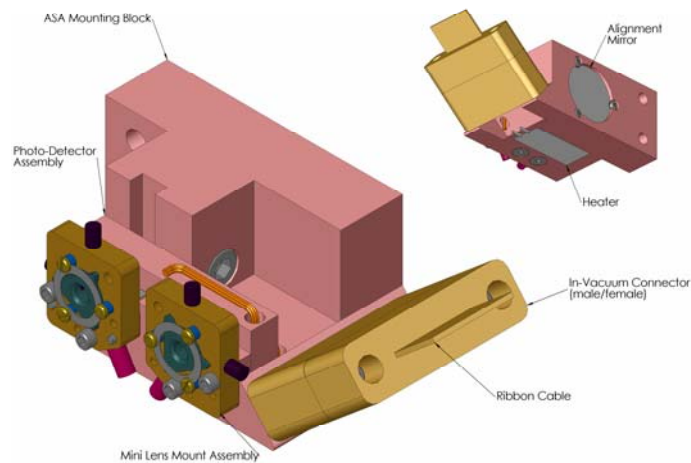
Figure 2.7.   Optical design for ASA.

Optimal positioning of the lens is monitored in the near-field by pulsing the QC laser at room temperature and measuring the beam pointing and angular divergence with a 250 μm MCT detector placed approximately 15 cm in front of the laser facet. The detector is on an optical rail for simple displacement between the two lasers. Lateral positioning of the lens is accomplished using 80-pitch adjustment screws and collimation is accomplished by adjusting the shim thickness between the ASA mounting block and the lens mount. Shims of various sizes are used to modify the angular divergence of the laser beam to the specified divergence of 4° FWHM.

Figure 2.7 also shows a mirror on the back of the ASA that is used for a reference beam. A HeNe laser is aligned to this mirror using an interferometric set-up that is illustrated in Figure 2.8. An interferometer is setup with a corner-cube retro-reflector at the end of the first arm and the ASA alignment mirror at the end of the second arm. The HeNe beam is first visually centered on the ASA alignment mirror and then the tilts of the beamsplitter and the pointing mirror are adjusted so that the HeNe laser beam in the second arm is made perpendicular to the ASA alignment mirror as indicated by the fringes on the screen. This adjustment allows alignment of the HeNe laser beam to within ±0.1 mrad of perpendicular to the ASA alignment mirror. The position of the HeNe alignment beam relative to the QCL beams at the detector mounted on the gantry robot arm 10 meters away from the ASA is measured by moving the ASA characterization cryostat assembly to allow the alignment beam to reach this detector. The ASA cryostat assembly is mounted on three radial v-groove kinematic mounts to allow accurate replacement of this assembly back to the same position.

Figure 2.8.   ASA Alignment Mirror Scheme

3.0   Control System & User Interface

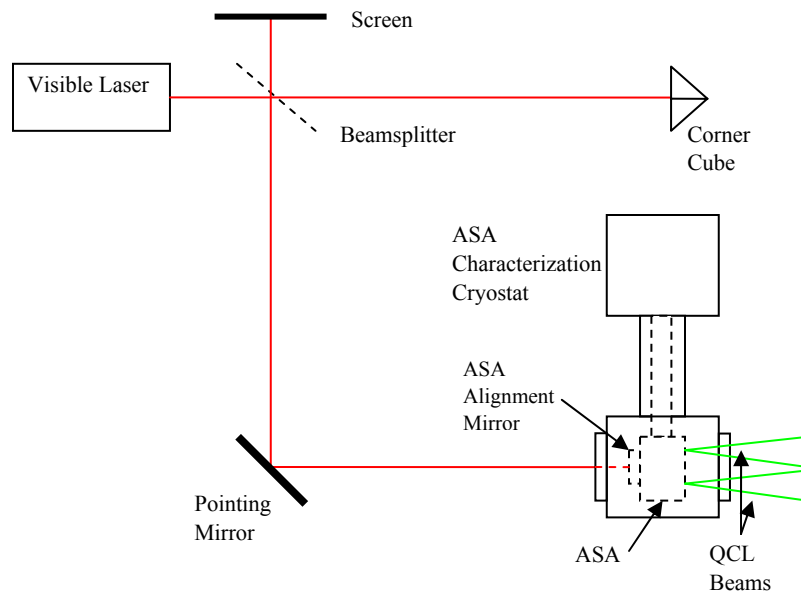The system includes a control computer (National Instruments Model NI-8176 Embedded controller in Model PXI-1000B) with a chassis rack mounted LCD monitor integrated with hardware for driving and monitoring the ASA laser output and controlling the ASA temperature for four ASA units. The Control System Software includes software for data collection, laser power control, and ASA thermal control with a GUI for data presentation as described in Section 3.1. PNNL installed the entire system into a half-height shippable instrument rack for easy transport and storage.

To minimize the size and cost of the instrument, PNNL incorporated a Keithley 7011S 40-channel multiplexer card along with a Keithley 7001 switch control mainframe so that a single current controller, a Keithley 238 High Current Source Measuring Unit, could be used to control all eight lasers sequentially. Two Lakeshore 332S temperature controllers with dual control loops are used for closed loop control of the ASAs. Since each unit has two control loops, one temperature controller can be used for two different ASAs. The first loop has a maximum heater output current of 1 A current and a maximum compliance voltage of 50 Volts; thus, the maximum heater output power for the ASA is 32 Watts since a 32 Ω resistive heater is applied to the ASA. Without the laser on, the typical heater power is 6.5 Watts to control the ASA temperature to 120 K when the cryostat temperature is maintained at 105 ºK. The second loop also provides a maximum heater output current of 1 A but the maximum compliance voltage is only 10 Volts; thus, the maximum power for a 32 Ω resistive heater is 3.1 Watts, which is not sufficient. Thus, the output power for Loop 2 is boosted for both temperature controllers with an auxiliary DC power supply. This design allows the temperature of all four ASAs to be controlled simultaneously.

3.1   User Interface Software

The software, which is written in LabView version 6.1, allows simple and reliable control of all the system instruments as well as automating certain processes. The software uses a GPIB (IEEE488.1) interface to communicate with the instruments in the half-height rack. These instruments control and measure the temperature of the four ASAs and the current and voltage of any one of the eight QC lasers that are mounted on the ASAs. A National Instruments 6025E 12-bit multipurpose I/O card is used to read the amplified voltage signal from the rear facet detector of the active QC laser.

The Alignment Laser software consists of two different windows. In the main window, all control and data monitoring is performed. The other window requires a password to access and is for setting all of the operational parameters, which are set at PNNL. Each ASA has a different settings window.

Figure 3.1 shows a screen shot of the main window. The arrows and labels in black describe the different areas. The "ASA Indicators" represent the ASA temperature and change colors to indicate status as described in Table 3.1. The "Laser Control" buttons also change colors to indicate status. The laser is red when it is not turned on, but it turns green when the laser is activated by left clicking on the "Laser control" button. The current to the laser is changed in –20 mA increments, and the indicator will flash

while the current is ramping up to its final value that is specified in the settings window. Once the laser reaches its set current, the "laser control" indicator changes to a steady green. The "Data Table" displays numerical values of the actual and target values for the active quantum cascade laser. The lasers are labeled by which ASA they are on (A, B, C, or D) and if they are the inner or outer laser on that ASA by the numbers 1 or 2 respectively. Temperature control of each ASA is turned on and off by clicking on the corresponding switch icon in the "Control Temperature" block. Error messages and messages indicating progress in turning on and off temperature control and lasers are displayed in the "Status" box. Clicking on the "STOP" button will cause a safe shut-down of the any active laser, temperature control, and this program. Finally, the "Menu" button gives password controlled access to the settings windows for the ASAs.
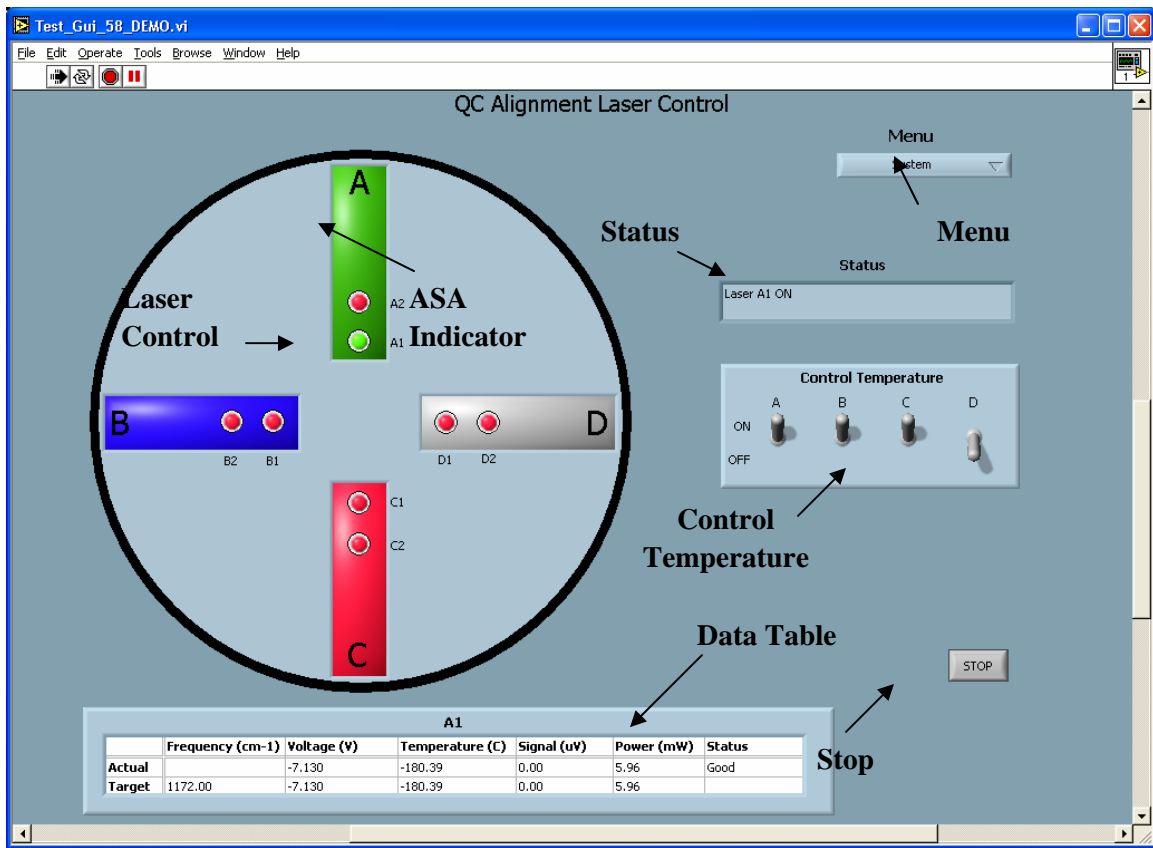
Figure 3.1.   Main Window for User Interface Software.

Table 3.1. ASA Indicator Color Code

ASA Color	Definition
Grey	ASA temperature is not currently controlled
Green	ASA temperature is within tolerance
Red	ASA temperature is above tolerance
Blue	ASA temperature is below tolerance

3.2   Cabling

The cabling for the Alignment Test configuration is illustrated in Figure 3.2. The external cables are fabricated by PNNL and are 30 ft. long since this length was requested by the Users. The internal cables are fabricated by the Using Subcontractor and are 75 feet long. PNNL could not use these internal cables inside their characterization cryostat due to their length. Instead, PNNL used a short auxiliary cable (about 2 feet) inside the cryostat.
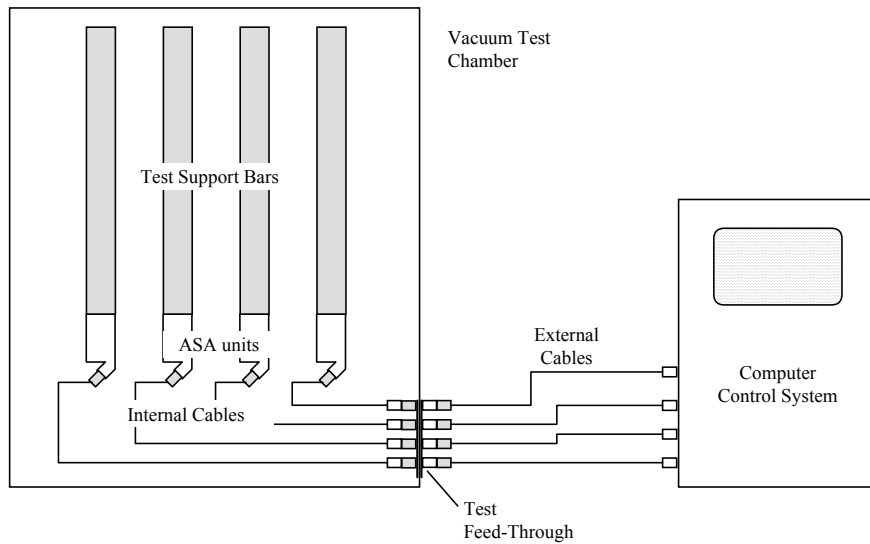
Figure 3.2. Cabling for Alignment Test Configuration

For the external cables, PNNL used 9 pairs of stranded conductors, 24 American wire gauge (AWG) with an overall shield (Belden 82509) for each of the ASA cables that come from the instrument rack and connect to the Vacuum Test Chamber. The internal cables, which are inside the Vacuum Test Chamber, were designed by the Using Subcontractor. PNNL recommended that the Using Subcontractor use cable designed for cryogenic environments and suggested 32 AWG twisted pair wire for signals (< 1amp) and 30 AWG wire for power cables (1 amp). These recommendations are to prevent thermal loading from the

wire and to minimize noise pick-up without impacting the signal levels. The Subcontractor, however, ended up using 24 AWG silver plated copper wire which led to a significant heat load.

Due to size constraints, the connector used for the ASA limited the system to 15 conductors and the pin assignments for this connector is illustrated in Figure 3.3. The system design required a four-lead temperature sensor measurement to eliminate the effect of lead resistance on the measurement. For the QC lasers, a four-lead measurement is also critical; however, due to the limited number of conductors, the ground for the two lasers had to be shared for both the current and the sensing leads.   The ground for the detectors also had to be common. For the ultimate performance, a design that allowed additional conductors is preferable especially to account for changes that occur during the lifetime of the project.
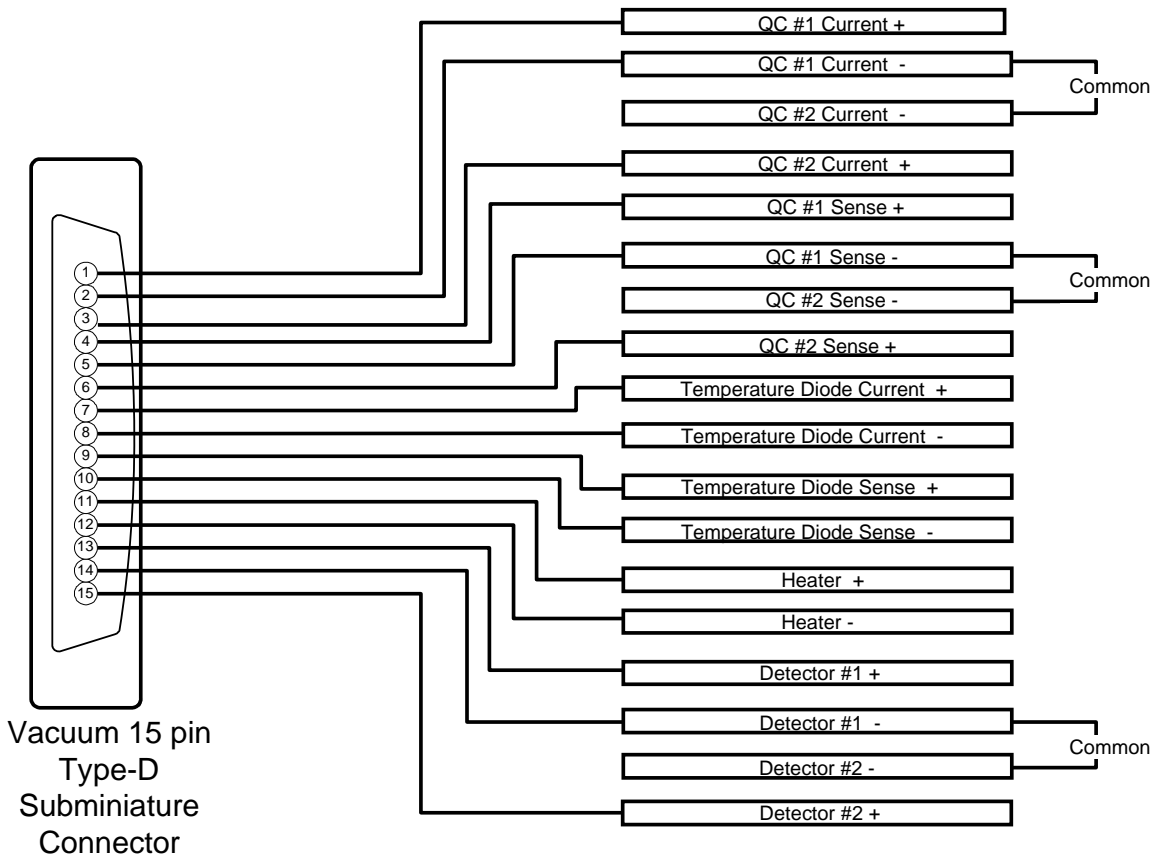
Figure 3.3. ASA Connector Assembly

3.4

The effect of the internal cable on the signal at PNNL is checked by inserting the cable outside the cryostat. PNNL did not observe a change in output power nor did it affect the compliance voltage.   The cabling should have little effect on the compliance voltage measurement since it is measured using a four-wire scheme at the laser. It did introduce an offset to the detector signal of -0.11 V; however this offset is simply subtracted from the signal since PNNL subtracts the background signal from the raw signal (see Section 4.5 for more details). Thus, PNNL carried out all of the characterization without using the internal cable since it did not appear to have an effect.

4.0   Far-field Characterization

The characterization involves measuring the irradiance for each QC laser relative to the visible reference laser as illustrated in Figure 4.1. PNNL used a commercial cryostat for cooling the ASAs. PNNL had the vendor modify the characterization cryostat so that two ASAs could be mounted simultaneously in order to speed up the testing process. Unfortunately, later modifications to the ASA design involved two stacked preamplifiers mounted to the top of the copper ASA mount, which prevented both ASAs from being mounted in the cryostat at the same time. Thus, PNNL has to vent the cryostat with dry nitrogen, mount a new ASA, and then pump down the system again every time a different ASA is tested. This step led to additional time required for testing.
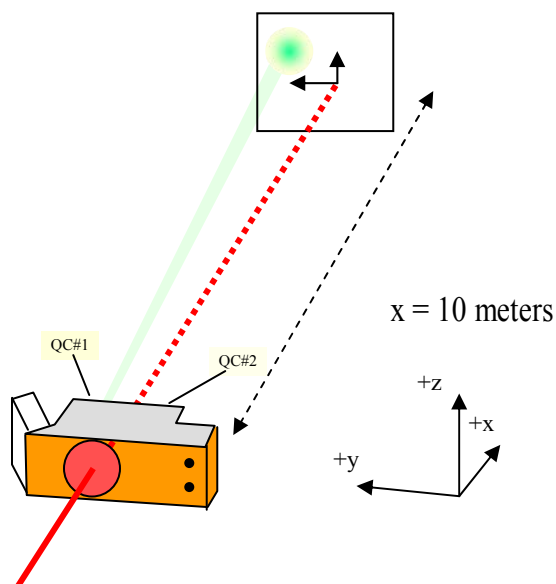
Figure 4.1.   Far-field Characterization Scheme. The z-axis represents the axis perpendicular to the quantum well layers of the QC lasers (referred to in text as vertical axis) whereas the y-axis represents the axis parallel to the quantum well layers (referred to in text as horizontal axis). The reference position of the alignment HeNe at the detector on the gantry arm is measured with the cryostat moved to the side as discussed in section 2.2.

4.1   Measurement Scheme

As shown in Figure 4.2, a large gantry style robot available at PNNL is used to map out the irradiance at a distance of 10 meters from the ASA. Due to the small signal levels at this distance, PNNL uses lock-in detection. A black anodized SR540 optical chopper in front of the cryostat modulates the output radiation. The lock-in amplifier is a Stanford Research Systems, SR830. PNNL used a Fermionics single element 1 mm diameter HgCdTe (MCT) detector (PV-12-1) along with a Stanford SR570 low current noise current pre-amplifier. The measurements are performed in an uncontrolled laboratory so that temperature and pressure fluctuations are present. PNNL observed noise on both the compliance voltage

and the rear facet detector signal when the robot is armed; thus, PNNL used an insulator, Sil-Pad, between the ASA and test support bar interfaces in order to electrically isolate the ASA.
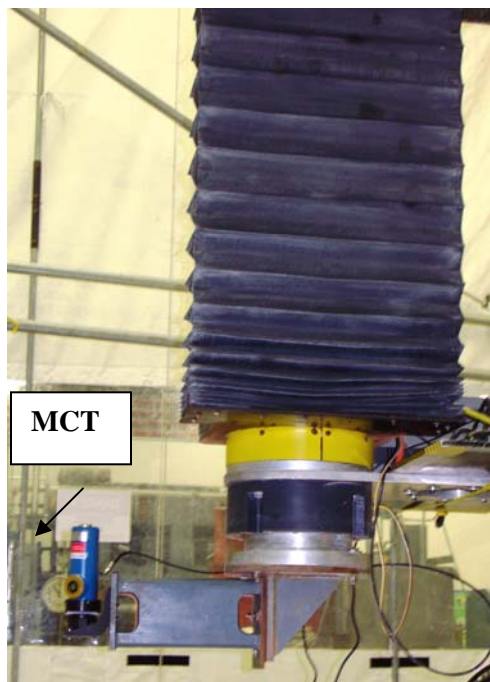
Figure 4.2.   Photograph of MCT Detector on Gantry Arm

PNNL looked at the stability of this measurement scheme. At one point, large fluctuations were noticed on the detector signal. Fluctuations that were as high as 20% could be observed, especially after refilling the detector with liquid nitrogen. Significant changes were also seen in the signal upon touching the copper ring around the detector window, which raised the window temperature. PNNL originally believed these fluctuations were due to fringing from reflections from the detector window. Thus, PNNL replaced the MCT window, which has a broadband AR coating, with a narrow-band AR coated window (see Section 4.3 for more details).

After PNNL replaced the detector window, PNNL measured the background signal using this scheme to determine the noise level in the system. For all of the data presented in this report, PNNL collected each data point by averaging six values using a 300 msec time constant on the lock-in amplifier. Figure 4.3 shows the background signal when the laser is not activated and the detector is kept at one spot for almost 12 minutes. The signal varies between 2.26 μV and 0.34 μV in which the mean background signal is 1.09 +/- .335 μV. All of the errors are reported as one standard deviation.
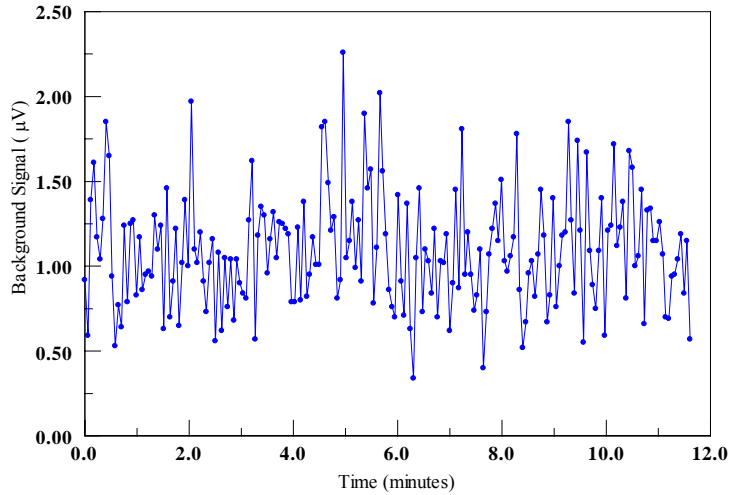
Figure 4.3.   Background signal fluctuations on the detector over a 12 minute time period.

For comparison, the laser is turned on and the signal is monitored over a similar time period. Figure 4.4 shows the signal fluctuations when the detector is kept in one spot and the laser is activated. The mean signal is 194.55 µV ± .58 µV. Thus, 95% of the values are within +/- 0.68% of the mean.
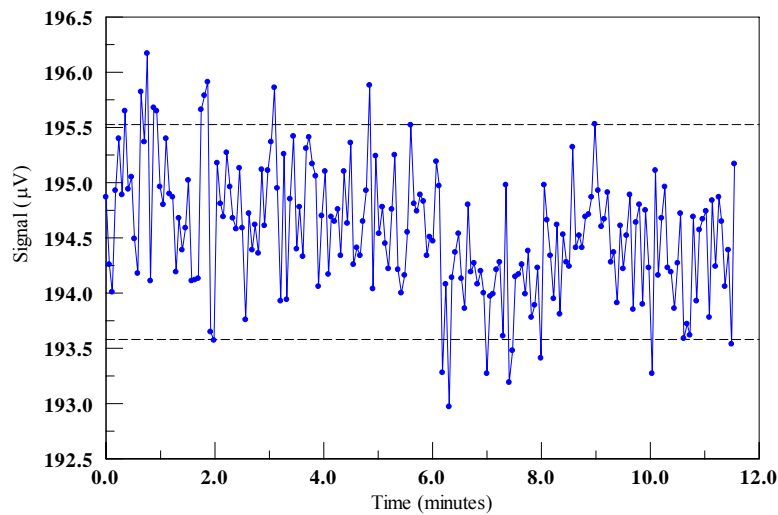
Figure 4.4.   Laser signal fluctuations on the detector over a 12 minute time period.

4.2   Vacuum window optical distortion calculations

The beam profile from each of the QC alignment lasers are measured with a vacuum window in the path of the laser beam, while in final use the beams do not pass through a window. It is essential that the measured beam profile can be used to predict the relative irradiance near the center of each beam for the final use to an accuracy of better than 1%. The most straight forward way to do this is for the vacuum

window to not change the relative irradiance near the center of the beams by more than 1% and it appears that this is achievable. The following effects are considered:

1) Angular changes due to the wedge of the window.
2) Etalon fringes imposed on the beam profile due to interference between the reflections at the two window surfaces.
3) Bending of the window due to the pressure differential and the resulting weak lens that is formed.
4) Optical power induced by temperature gradients.

The first of these effects is independent of the size of the vacuum window, the second depends on the window thickness and residual reflectivity, and the last two depend on both the window thickness and clear aperture. The required clear aperture of the window is determined by the need to inter-compare the beams from different alignment source assemblies (ASAs) that each produces a pair of laser beams separated by 1 ± 0.1". The parameters for the window assumed for these calculations are in Table 4.1 and similar to ISP Optics model ZC-W-76-8 with a V-type antireflection coating from Lohnstar Optics.

Table 4.1. Vacuum Window Parameters

Parameter	Value
Material	ZnSe
Diameter	3.000" +0/-0.005"
Unsupported Diameter	2.75"
Thickness	12.7 mm
Parallelism	3 arc minutes
Flatness	1/20 wave at 10.6 microns
Surface Finish	60/40
Reflectivity w/ AR coating	0.15% per surface
Refractive Index	2.415

4.2.1   Window wedge

A wedge of the window of 3 arc minutes (or 0.05 degrees) and the beam perpendicular to the first surface gives a deflection after the second surface of the window of

$$\arcsin(n \cdot \sin(0.05°)) = 0.12°$$

where n is the refractive index. The specifications state that the laser beams need to be aligned to ±0.1° from perpendicular to the mounting surface. This is slightly larger than the ±0.1° specification, which

would require the windows to be parallel to better than 2.4 arc minutes. A tighter specification was not required so that PNNL regarded this specification as sufficient.

4.2.2 Etalon Fringing

The transmission of a solid etalon with reflectivity R is expressed as (Hernandez 1986).

$$\frac{(1-R)^2}{1+R^2-2R \cdot \cos(\delta)}$$

where δ, the round-trip phase difference in the etalon, is given by

$$\delta = \frac{4\pi n d}{\lambda} \cos(\theta)$$

where n is the refractive index, d is etalon thickness, λ is the vacuum wavelength, and θ is the angle of incidence from normal. These equations assume that the loss due to absorption and scatter is zero. Using the reflectivity in Table 4.1, the transmission ranges from 99.4% to 100%. Reflectivity of 0.25% gives a minimum transmission of 99% and this is the maximum allowable reflectivity that will ensure that ratios of irradiances between pairs of lasers that we measure will match to 1% in the final use. The free-spectral-range (FSR) of the 12.7 mm thick window is 0.16 cm^{-1}. If each laser were tuned to the closest maximum transmission or minimum reflection, then it would be possible to reduce the effect of the window on the center of the beam. However, if this is done at normal incidence, then for a wavelength of 8 µm, the first minimum in transmission is at 0.65° and the next maximum is at 0.93° for a thickness of 12.7 mm. In conclusion, attempting to correct for window fringing by tuning the wavelength would only work over a small part of the beam. Fortunately, the specified reflectivity of an AR coating from Lohnstar Optics is adequate to meet a 1% relative radiance specification.

4.2.3 Power of a bent window

A simply supported window with a pressure differential ΔP across it has an axial deflection as a function of radius, *w(r)* given by (Hearn 1999)

$$w(r) = \frac{3\Delta P (1-v_P^2)}{16EL^3} \cdot \left[\frac{5+v_P}{1+v_P} a^2 - r^2 \right] \cdot \left[a^2 - r^2 \right]$$

where L is the thickness of the window, a is the radius at which the window is simply supported, v_P is Poisson's ratio, which is 0.28 for ZnSe, and E is the elastic modulus of the window, which is 70.3 GPa for ZnSe. With the values in Table 4.1 the maximum deflection is 0.75 µm for a 12.7 mm thick window. The curvature of the surfaces near the center of the window is (Hearn 1999)

$$\frac{1}{ROC} \cong \frac{3(1-v_P)(3+v_P)a^2\Delta P}{4EL^3}$$

where ROC is the radius of curvature. This combination of vacuum, bent window, and air form a weak lens with a focal length of (Hearn 1999)

$$\left[\frac{(n_{air}-1)}{ROC} + \frac{L}{ROC^2}\cdot\frac{(n_w-1)^2}{n_w}\right]^{-1}$$

where n_{air} is the refractive index of air and n_w is the refractive index of the window. This gives a focal length of 2.5 x 10^3 km for the 12.7 mm thick window. The power of this weak lens, which is roughly 50 mm from the virtual source of the laser beam, will change the divergence by about one part in 10^7, which is negligible.

4.2.4   Temperature Gradients

Others have modeled and measured the distortions in a fused silica vacuum window that was 5 cm thick and 32 cm in diameter where there was a cold shield at about 100°K inside the vacuum system (Hearn DR 1999). The radiative cooling of the vacuum surface of the window resulted in axial and radial temperature gradients in the window and the radial gradients were the source of the dominant optical distortions of the window. For the planned setup to test the QC alignment lasers, these effects are expected to be much smaller because of the following reasons:

1) ZnSe is highly transparent at thermal wavelengths so its emissivity is very low compared with that of fused silica which is 0.74.
2) The thermal conductivity of ZnSe is almost 10 times larger than that of fused silica.

In contrast, the change in refractive index with temperature of ZnSe is about 7 times larger than for fused silica. PNNL implemented Hearn's heat flow solution in Mathcad and confirmed the worksheet by calculating the results for the fused silica window of Hearn. Using this Mathcad worksheet, but changing the window dimensions and thermal properties to that of ZnSe, assuming an effective emissivity of 0.1, and increasing the effective temperature of the vacuum chamber from 271°K to 280°K, PNNL calculated the temperature distribution in the window. The use of an effective vacuum chamber temperature was used to include the effects of fields of view and emissivities of the components in the vacuum chamber. This parameter was chosen by Hearn to match the calculations to axial temperature difference measured with thermocouples. The assumed effective temperature and emisivity of ZnSe seem to be very conservative assumptions. The resulting maximum calculated temperature difference of the window from ambient is -0.02°K and the resulting maximum difference in optical path through the window is 31.5 nm for an effective focal length of -20 km. Thus the thermal gradients should not be a problem.

These calculations justify that the use of a window should not distort the beam irradiances relative to the actual use without the window. The calculations do show that the AR coating needs to be better than 0.25% reflectivity per surface, but the window that PNNL used actually had an AR coating of < 0.15% per surface with a V-type AR coating.

4.3   Optical Fringing

PNNL used shims of varying thickness to adjust the angular divergence of the output beam. When the lens is near the laser facet, significant fringing on the beam profile is observed. Figure 4.5 below shows the far-field signal for ASA #C1 with two different shim thicknesses using a 3.2" detector grid spacing at 10 m. Both grids are plotted relative to the gantry robot position. Figure 4.5a shows the beam profile using a shim thickness of .003". The output power at -550 mA using this configuration is approximately 11 mW, but extreme fringing is observed in the profile. On the other hand, Figure 4.5b shows the profile using a shim thickness of .009" so that the lens is significantly farther away from the laser facet. The output power at -550 mA using this configuration is reduced to 3.3 mW since the lens is farther away from the laser. This shim spacing enables a smoother profile but the angular divergence is still too narrow to meet the specifications. A cut along the horizontal axis demonstrates the FWHM is 2.2° and a cut along the vertical axis has a FWHM of 2.7°.
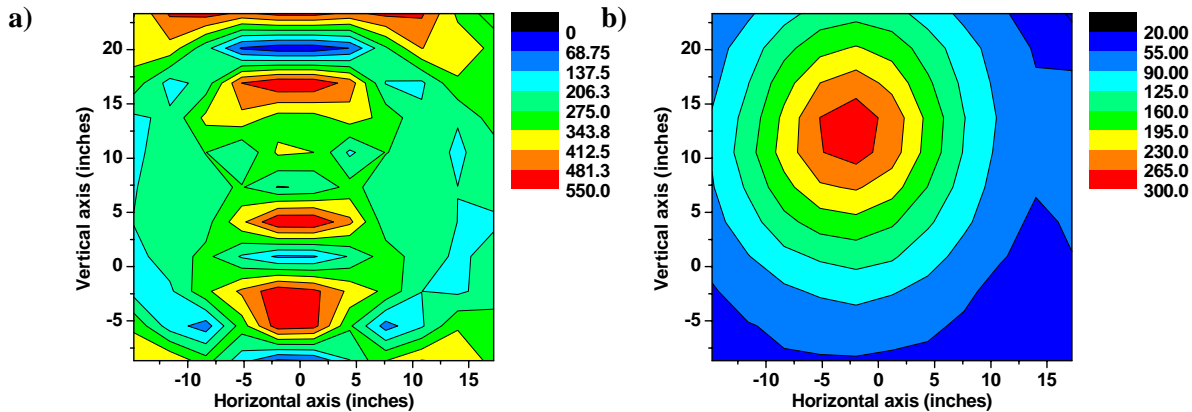

Figure 4.5.   Contour plot of the far-field beam profile at a distance of 10 meters for C1 with (a) .003" shims and (b) .009" shims using a 3.2" spacing (apr19002).

To extend the angular divergence, PNNL increased the shim thickness as illustrated in Figure 4.6. Figure 4.6a shows the beam profile when the shim thickness is .010". The beam is highly elliptical, for the beam width is 2.5° along the horizontal but 5.0° along the vertical. By reducing the shim thickness to .0095", PNNL obtained a beam profile that more closely matches the specifications as demonstrated in Figure 4.6b. The beam is slightly elliptical with a beam width of 3.2° in the horizontal direction and 4.1° in the vertical direction. This configuration appeared to be a good compromise to meet the specifications. PNNL also examined other lasers and verified that similar trends were present.
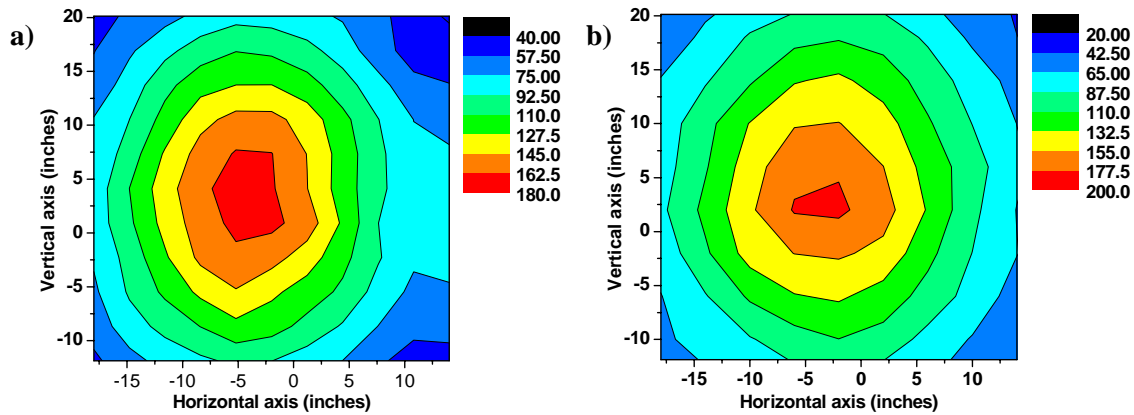
Figure 4.6. Far-field beam profile for C1 with (a) .010" shims using a 3.2" step size and with (b) .0095" shims using a 4" spacing.

PNNL examined the near-field profile using an IR camera without a lens and with the camera close to the cryostat window to observe the fringing. Figure 4.7a shows a typical beam pattern that is observed when the Ge lens is close to the facet of the laser (i.e. with an .002" shim). By positioning the lens farther from the laser facet, PNNL obtained a smoother profile. Figure 4.7b shows the near-field signal for ASA D2 with .009" shims. When the lens is closer to the laser facet, a circular ring pattern appears in which the rings have roughly equal intensity. These rings appear whether or not the AR coated window on the cryostat is used because when the lasers operate pulsed at room temperature, a MCT detector that is moved along the optical axis shows similar fringing and the window is not present.
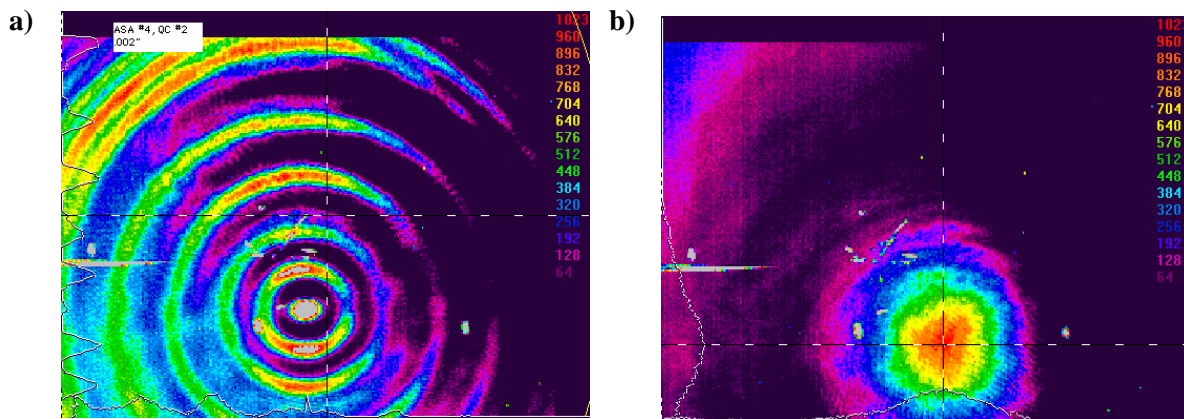
Figure 4.7. Near-field profile for (a) ASA B2 with .002" shims and (b) ASA D2 with .009" shims.

This fringing is most likely due to spherical aberrations in the germanium lens, which occur when all the rays do not focus to a single point. Spherical aberrations can be a problem with QC lasers due to the beam's high divergence angle; QC lasers have a typical angular divergence of 20-30° in the plane parallel to the layers and 60° in the plane perpendicular to the layers. Thus, the paraxial rays are brought to a focus and then interfere with rays further out in the bundle that have already passed through their closer

focal points and are beginning to spread out again. Their contribution to the image shows up as a set of concentric rings in which the outermost ring corresponds to rays passing through the outermost portion of the lens that have the shortest focal lengths.

When PNNL uses a step size smaller than 3" to measure the beam intensity in the far-field, additional fringing atop the beam profile becomes apparent for configurations when the angular divergence is greater than 1°. When the angular divergence is narrow (i.e. around 1°), a very smooth profile is obtained. Figure 4.8a shows the far-field signal for D1 with .006" shims at -440 mA. This plot is a 10" by 10" grid with 1" step size. A very smooth profile is measured. The beam is symmetric with a beam width of about 0.75 ° in both the horizontal and vertical directions. Figure 4.8b shows a very smooth profile even with a 0.1" spacing.   The angular divergence, however, is too narrow and needs to be increased.
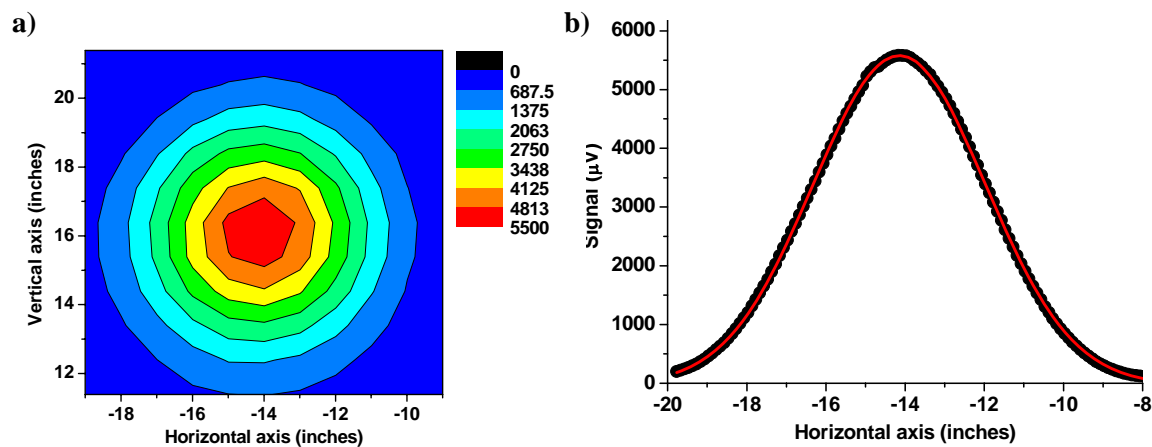
Figure 4.8.   Beam profile for D1 with .006" shims. a) Contour plot for a 10" by 10" grid with a 1" spacing. b) A horizontal cut along z = 16.25" in 0.1" increments. The black circles correspond to the data, and the red line corresponds to a Gaussian fit of the data.

Fringing, however, begins to appear as the divergence increases. Figure 4.9 shows a cut along the horizontal axis for D1 with .009" shims using a 0.4" spacing that demonstrates fringing atop the beam profile. The beam divergence is only 2.3° but fringing appears. This fringing did not disappear when PNNL implemented a narrow-band AR coated detector window optimized for the QCL wavelength.

4.9
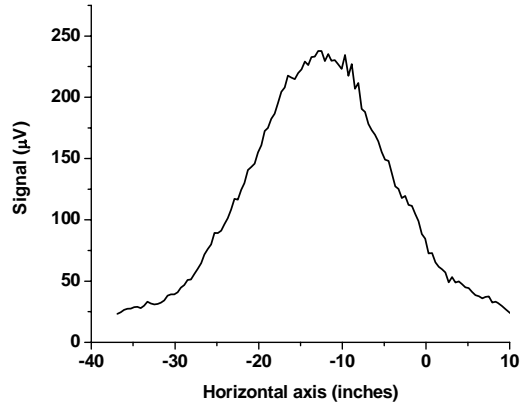
Figure 4.9. Horizontal cut for D1 with .009" shims in 0.4" increments.

This fringing appears to be stable at least within the error of the measurement. PNNL recorded data at three different times over a 2 hour time period for a cut along the horizontal axis for one of the lasers. The mean standard deviation for all three cuts is 0.79 µV. For the data that is greater than 100 µV, the mean normalized standard deviation is ± 0.72% for the three cuts. Figure 4.10 shows the results. The normalized standard deviation is greater in the wings since the signal is lower. For all of the grids, PNNL made sure the signal was greater than 100 µV to avoid larger percent fluctuations. In fact, the average signal from the grids is 171 µV.

Figure 4.10. The mean signal (top), standard deviation (middle), and normalized standard deviation (bottom) for a cut along the horizontal axis for C2.

4.10

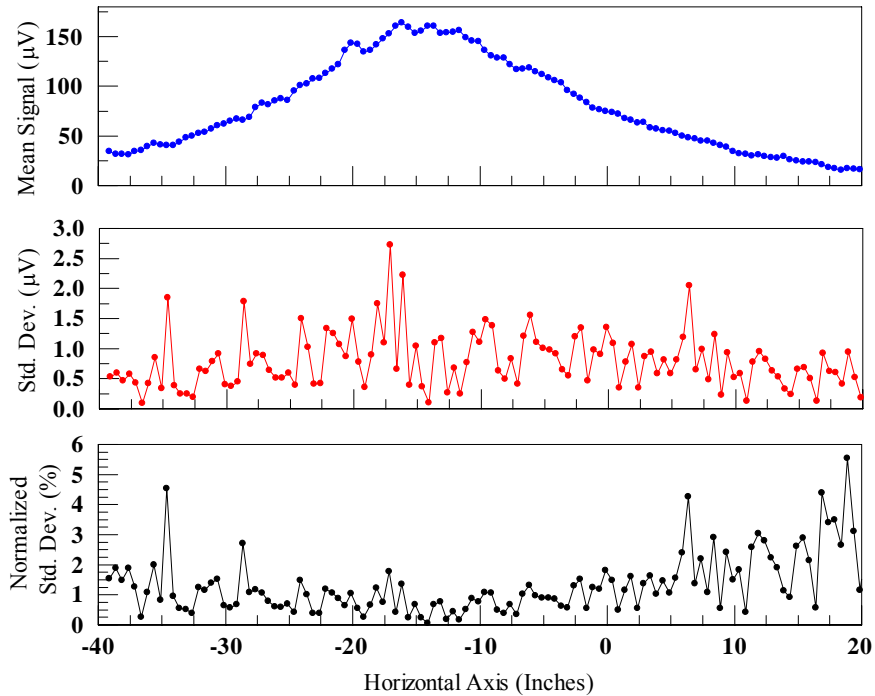Table 4.2 shows the final shim thicknesses used for each laser and the angular divergences that are achieved.

Table 4.2. Horizontal and Vertical Angular Divergences for each ASA along with the shim thickness.

ASA	Shim Thickness	Horizontal Angular Divergence	Vertical Angular Divergence
A1	.003"	3.3	3.6
A2	.003"	3.7	4.0
B1	.0085"	3.4	4.0
B2	.008"	3.1	3.5
C1	.0105"	3.0	3.2
C2	.0095"	3.1	3.8
D1	.0095"	3.4	3.9
D2	.0095"	3.6	4.3

Figures 4.11, 4.12, 4.13, and 4.14 show the horizontal and vertical cuts for each laser on ASAs A, B, C and D, respectively, using the shim values provided in Table 4.2.

Figure 4.11. Horizontal (left) and Vertical (right) Cuts for ASA A1 (black) and A2 (red).

4.11

Figure 4.12. : Horizontal (left) and Vertical (right) Cuts for ASA B1 (black) and B2 (red).

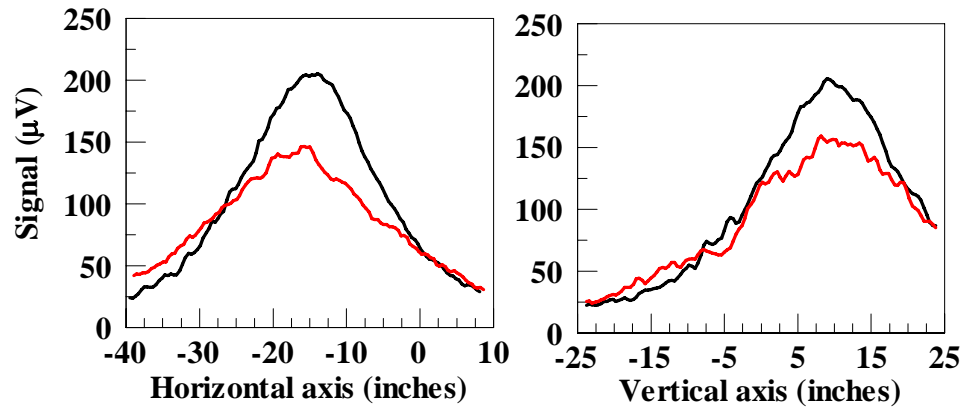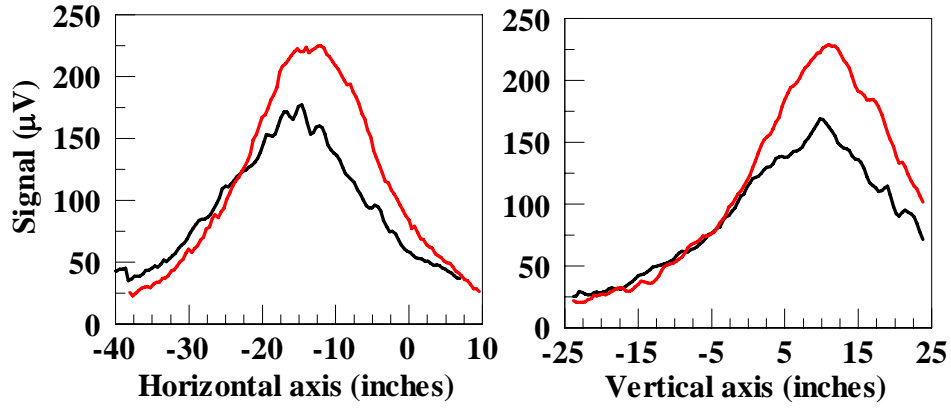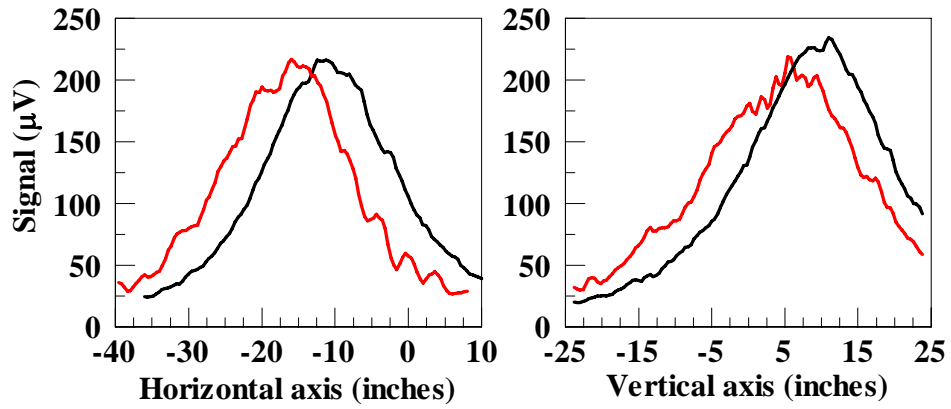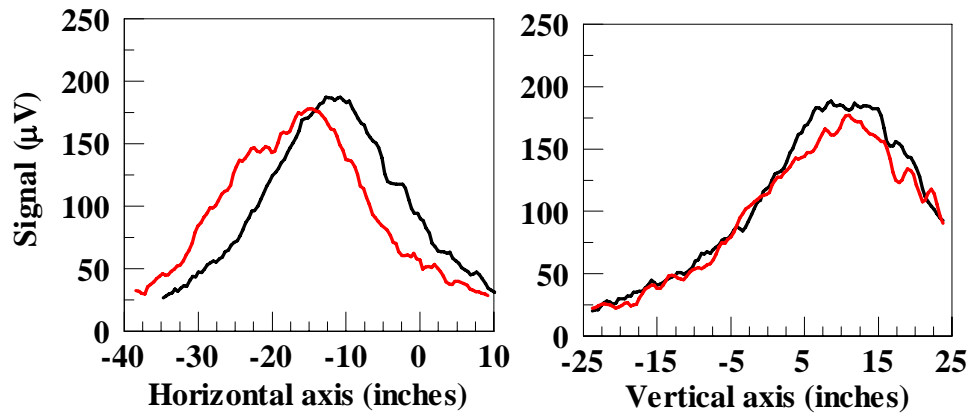**Figure 4.13.** : Horizontal (left) and Vertical (right) Cuts for ASA C1 (black) and C2 (red).

Figure 4.14. : Horizontal (left) and Vertical (right) Cuts for ASA D1 (black) and D2 (red).

4.4   Thermal Hysteresis

PNNL observed varying degrees of thermal hysteresis in the output power of the lasers. In particular, PNNL noticed strong thermal hysteresis effects for D1. For this laser, the power depended strongly on the initial temperatures of the cryostat and the ASA. When the ASA was cooled all the way down to 80 K, the output power of ASA D1 was higher than when the ASA temperature was not allowed to go much below 120 K. For example, when the initial ASA temperature was 209 K and the temperature did not go below 115 K, the output power at -459 mA was only 1.92 mW and only 2.04 mW at -468 mA. The temperature of the cryostat was then cooled to 80K and the ASA to 90.7 K and then heated back to 120 K. The power increased so that the output power at -459 mA increased to 2.37 mW and 2.57 mW at -468 mA (about a 25% increase). PNNL then cooled the ASA all the way to 83.3 K and then heated it back to 120 K and the output power was even higher. At -459 mA, the output power increased to 2.57 mW and at 468 mA, the output power increased to 2.75 mW (about another 8% increase). Then the ASA and cryostat were heated to 160 K and cooled slowly back down to 120 K. The power decreased so that at -459 mA, the power decreased to 2.26 mW. When the ASA and cryostat were cooled back down to 80 K, the power increased back to 2.55 mW at -459 mA. The chart below shows the observed effects.

Table 4.3. Thermal Hysteresis Effects for ASA D1

Current	Power	Date	Signal	
Cooled ASA to 97 K				
-468	2.48	7/28	-.726	
Cryostat and ASA kept below 105 K				
-468	2.73	7/29	-.727	
-459	2.52	7/29	-.712	
ASA and cryostat at 209 K upon cool-down and temperature dropped to 115 K				
-468	2.04	7/30	-.706	
-459	1.91	7/30	-.686	
-489.5	2.44	7/30	-.744	
Cooled cryostat to 80 K and ASA to 90 K				
-489.5	3.06	7/30	-.757	
-459	2.37	7/30	-.707	
-468	2.57	7/30	-.721	
Cooled cryostat to 80K and ASA to 83 K				
-459	2.57	7/30	-.712	
-468	2.75	7/30	-.730	
Heated cryostat and ASA to 160 K				
-459	2.26	7/30	-.681	
Cooled ASA and cryostat to 80 K				
-459	2.55	7/30	-.694	
Cryostat and ASA heated to 300 K and cooled to 118 K				
-490	2.20	7/31	-.735	
-509	2.51	7/31	-.759	

PNNL did not have time to thoroughly investigate the thermal hysteresis effects due to the tight delivery schedule. Thus, PNNL chose to use a consistent method for cooling down the ASAs. Since it was unclear if the Users would be able to reach a temperature below 120 K, PNNL chose to always use a soft landing to 120° K and not let the temperature drop far below 120° K. Thus, the heater to the ASA was turned on once PNNL began cooling down the cryostat to prevent the temperature from falling below 120° K.

4.5 On-board Photodetectors

PNNL installed photodetectors on the ASA to monitor the rear facet of each of the lasers. The original design involved using photovoltaic HgCdZnTe (MCZT) detectors that operate from 220 – 240 K and did not require a bias. Due to the change in operating temperature, PNNL had to change to cryogenically-cooled photodetectors. Thus, PNNL switched to photovoltaic MCT detectors from Fermionics with a 1 mm diameter. Two amplifiers were added to the ASA but no bias could be applied due to the limited number of conductors available. Linearity was observed over the limited dynamic range tested. The responsivities are shown below in Table 4.4.

Table 4.4. Responsivities for the rear-facet detectors.

ASA	Responsivity (V/mW)
A1	-.0614
A2	-.0680
B1	-.0898
B2	-.0702
C1	-.0528
C2	-.0575
D1	-.0708
D2	-.0371

PNNL incorporated a background subtraction scheme to eliminate dark signal from the photodetectors. During the turn-on procedure for the lasers, the software stops the system at -200 mA, which is below threshold for each laser. Once the ASA temperature reaches 120 K, the program averages signal from the rear facet detector which is subtracted from the signal collected at the set current and presented in the data table.

Unfortunately, these detectors did not seem to provide a good indicator of the output power from thermal hysteresis effects. As shown in Table 4.3, PNNL did not observe a change in the detector signal even when the output power changed due to the initial temperature of the ASA. The detectors do, however, provide a good indicator that the lasers are emitting light.

4.6   Final Characterization

The characterization involved collecting data in an 8" by 8" grid for each laser. Each grid has a total of 441 points since PNNL used a 0.4" spacing in order to observe any fringing present in the beam profile. Initially, PNNL measured six grids per laser in which PNNL collected half the data by moving the gantry robot along the horizontal axis and the other half by moving the gantry robot along the vertical axis. After the characterization for all four ASAs is completed, PNNL wrapped all of the exposed areas of one of the ASAs in the thermal tape that was provided by the Using Subcontractor. This low emissivity tape is necessary to reduce the radiative heating of the ASA in the Using Subcontractor's Alignment Test configuration. After PNNL wrapped one of the ASAs in thermal tape and retested the characterization, they observed changes in the characterization. This change could have occurred from the lens being bumped so PNNL then staked all of the screws on the lens mounts with an epoxy (3M Scotch-Weld Epoxy Adhesive 2216 -grey). After all of the ASAs are wrapped in thermal tape, PNNL repeated the characterization for all eight lasers, but limited the data collection to only two grids per laser in order to meet the scheduling requirements. Thus, the final irradiance values for the grids are calculated by averaging two different data sets. Since this data is all collected on the same day, the error for the grids is sometimes smaller than the original characterization. Thus, PNNL used both the original and the final characterization to estimate the error for the grids. The mean normalized standard deviation for all the lasers is shown in Table 4.5. Thus, it varied from 0.86% to 1.55%.

Table 4.5.   Percent errors for the irradiance maps.

ASA	Mean Normalized Standard Deviation (%)
A1	0.92
A2	1.34
B1	1.29
B2	1.41
C1	.86
C2	1.22
D1	1.55
D2	0.89

The final grids relative to the HeNe beam are shown in Figures 4.15, 4.16, 4.17, and 4.18. Table 4.6 shows the final parameters for each laser with an ASA temperature of $120.00 \pm .01$ K. PNNL measured the frequency using an OPAG FTIR with a resolution of 0.5 cm^{-1}.   PNNL also examined how the output power changed with temperature and current; these results are included in Table 4.6.
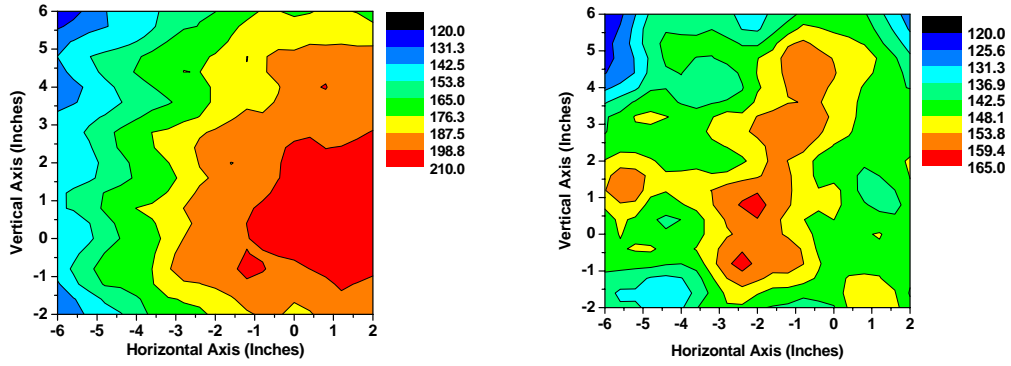
4.15

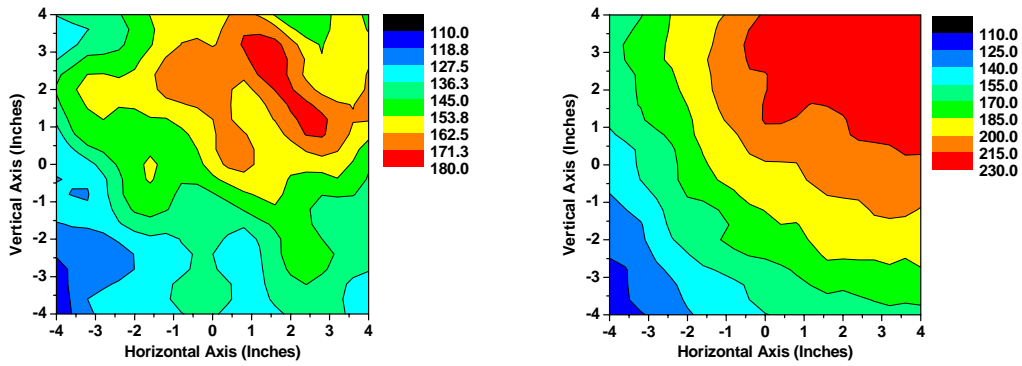**Figure 4.15.** Irradiance map for A1 (left) and A2 (right).

Figure 4.16. Irradiance map for B1 (left) and B2 (right).
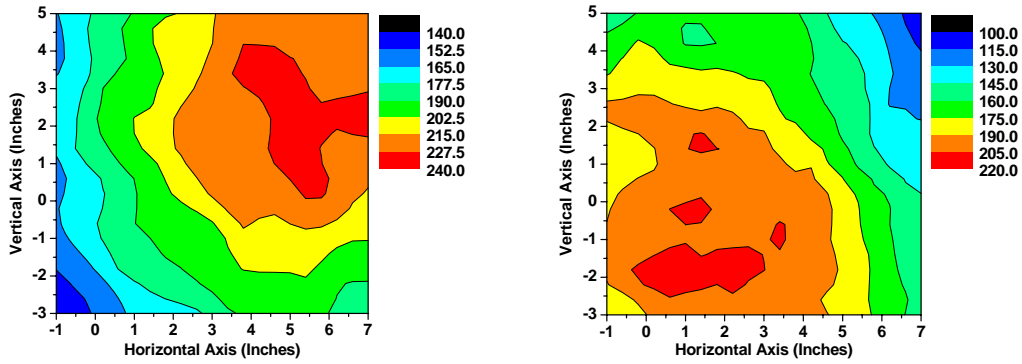

Figure 4.17. Irradiance map for C1 (left) and C2 (right).

4.16
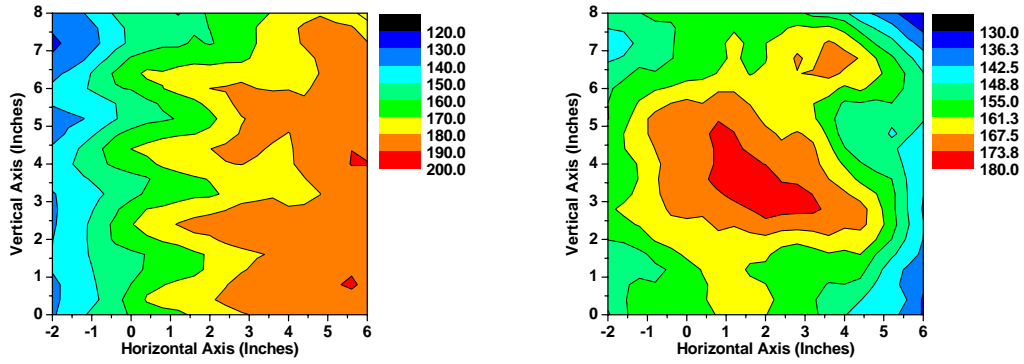
Figure 4.18. Irradiance map for D1 (left) and D2 (right).

Table 4.6. Parameters for the Alignment Lasers.

ASA	Operating Current (mA)	Output Power (mW)	Frequency (cm^{-1})	Slope Efficiency (mW/mA)	mW/K
A1	-481	2.71	1180.7	-.066	-.371
A2	-423	2.87	1181.0	-.029	-.109
B1	-459	2.80	1180.9	-.015	-.075
B2	-409	2.75	1181.1	-.022	-.051
C1	-459	2.85	1180.7	-.035	-.110
C2	-478	2.68	1180.0	-.015	-.066
D1	-508	2.75	1179.9	-.015	-.081
D2	-548	2.75	1180.1	-.014	-.099

5.0   Alignment Test

PNNL shipped the entire Laser Alignment System to the Using Subcontractor on September 24, 2004 along with an operations manual. In January 2005, the Using Subcontractor mounted ASA #A onto their test support bar and performed several thermal tests to verify that the ASA could be properly cooled down in their vacuum test chamber. Their initial check showed they had trouble cooling down the ASA to 120K. In fact, they measured a 100° C difference between the laser bar and the ASA. They discovered that this thermal problem was predominantly due to poor mechanical contact since the wrong screws were used to attach the ASA to the support bar. After this test, however, they vented the chamber when the ASA was still at cryogenic temperatures so that frost formed on the ASA. This step did not appear to cause any damage.

Another problem that arose is contamination in their vacuum test chamber. Since ASA #A was in the chamber during this contamination and at cryogenic temperatures for about 20 hours, some contamination may have occurred on ASA #A. After the contamination problem was solved and the ASA was mounted properly, they performed another thermal test that showed erratic temperature readings for the ASA. The temperature would oscillate by ±0.2K and the temperature could not be controlled to ±0.01K. This additional noise most likely results from the cable used in their set-up. Thermal EMF voltages appear whenever there is a temperature gradient across a piece of voltage lead. Fortunately, the polarity of the sensor can be reversed and the temperature controller has a thermal correction algorithm that takes the average of the positive and negative sensor readings. This step removes effects due to thermal EMF voltages since it has the same polarity regardless of the current direction.   The original version of the software had this algorithm turned "OFF" so an updated version is sent that now has this algorithm turned "ON" as the default. This feature is useful for eliminating emf noise by reversing the current of the resistive temperature sensor and averaging the voltage readings.

On March 20, 2005, the Using Subcontractor completed the pupil alignment test. The testing proceeded fairly well although two of the laser beams were obscured (A2 and B2). The rear facet detectors for both of these lasers verified the lasers were working. Unfortunately, the laser beams were blocked due to installation performed by the Using Subcontractor in which extra multi-layer insulation (MLI) tape had been wrapped over the end of the ASA and extended over the beam region and blocked the beam path. They were able to gather enough good data to make a fairly accurate assessment of pupil alignment based on the irradiance maps that were provided. The analysis of the data from the pupil alignment test was quite favorable so they were able to satisfy the goals of this test even without two of the beams. Basically, the alignment was satisfactory and everyone was pleased with the outcome of this test. Although they had plans to repeat this test with precautions to avoid blocking any of the lasers, they later canceled this effort due to the encouraging results from this preliminary alignment test along with some more recent test results on associated hardware provide substantial confidence that system alignment is quite close to nominal. Due to the projected costs and delays associated with a repeat of the alignment test, they decided it wasn't necessary.

6.0   References

Hearn DR 1999. "Vacuum window optical power induced by temperature gradients." Paper 3750-37, for presentation at SPIE Conference: Earth Observing Systems IV, Denver, CO.

Hernandez G 1986. "Fabry-Perot Interferometers." Cambridge University Press, Cambridge, New York, New Rochelle, Melbourne, Sydney, page 12.

Distribution

No. of
Copies

No. of
Copies

OFFSITE

LTC Ariel Cuadrado
United States DOE
NNSA/NA-22
1000 Independence Ave. SW
Washington, DC 20585

Dr. Rhys M. Williams
United States DOE
NNSA/NA-22
1000 Independence Ave. SW
Washington, DC 20585

Dr. David Berry
United States DOE
NNSA/NA-22
1000 Independence Ave. SW
Washington, DC 20585

Mr. Ralph Hastings
United States DOE
NNSA/NA-22
1000 Independence Ave. SW
Washington, DC 20585

Mr. Eric Sander
United States DOE
NNSA/NA-22
1000 Independence Ave. SW
Washington, DC 20585

Mr. W. Randy Bell
United States DOE
NNSA/NA-22
1000 Independence Ave. SW
Washington, DC 20585

Professor Henryk Temkin
Program Manager
DARPA, MTO
3701 N. Fairfax Dr.
Arlington, VA 22203-1714

ONSITE

23 **Pacific Northwest National Laboratory**

Broocks, BT	K5-25
Bruckner-Lea, C	K5-25
Cannon, BD	K5-25
Clemmer, RG	K8-29
Dudder, GB	K8-29
Hatchell, BK	K5-22
Myers, TL	K5-25
Schultz, JF (10)	K5-25
Sharpe, SW	K8-88
Stewart TL	K5025
Wojcik, MD	K5-25
Information Release Office (3)	K1-06